ACS APPLIED MATERIALS & INTERFACES

Research Article

www.acsami.org

Facile Template-Free Fabrication of Hollow Nestlike α-Fe_2O_3 Nanostructures for Water Treatment

Zhenhua Wei,*[,†,‡] Ronge Xing,[†] Xuan Zhang,[§] Song Liu,[†] Huahua Yu,[†] and Pengcheng Li*[,†]

[†]Institute of Oceanology, Chinese Academy of Sciences, Qingdao, 266071, China

[‡]University of Chinese Academy of Sciences, Beijing, 100039, China

[§]College of Chemical Engineering, Qingdao University of Science and Technology, Qingdao, 266042, China

Supporting Information

ABSTRACT: Hollow nestlike α-Fe_2O_3 spheres were successfully synthesized via a facile template-free, glycerol-mediated hydrothermal process employing microwave heating. The product was characterized using X-ray diffraction, field-emission scanning electron microscopy, transmission electron microscopy, and nitrogen adsorption measurements. The as-prepared product was found to consist of hierarchically nanostructured spheres assembled of nanorod subunits. The effect of the relative amount of glycerol in the reaction system on the composition and morphology of the products was systematically studied, and a possible formation mechanism of the hollow nestlike spheres was proposed. Because of their large surface area and unique mesoporous structure, we investigated the potential application of the hollow α-Fe_2O_3 spheres in water treatment. With maximum removal capacities of 75.3, 58.5, and 160 mg g^{-1} for As(V), Cr(VI), and Congo red, respectively, these novel nanostructures have the potential to be used as low-cost and efficient adsorbent materials for the removal of toxic metal ions and organic pollutants from water.

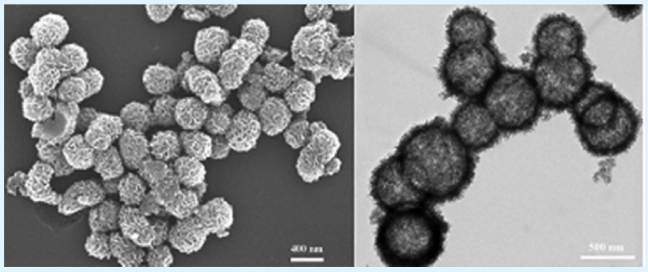

KEYWORDS: *α-Fe_2O_3, hollow nanostructures, adsorption, water treatment, heavy-metal ions, Congo red*

1. INTRODUCTION

The environmental and health issues associated with contaminated waters have led to increasing public concern as population density and industrialization have increased globally.[1] Currently, nanomaterials and nanotechnology have garnered worldwide attention for their application in environmental remediation and pollution control, because nanostructured surfaces offer large surface areas and rich valence states that provide enhanced affinity and adsorption capability toward pollutants.[2−5] For example, the development of various nanoscale iron oxides with uniform sizes for the removal of toxic heavy metal ions and organic pollutants from wastewater has accelerated recently, because of the lost cost, abundant availability, and environmentally benign characteristics of these nanoscale materitals.[6−9] Recently, three-dimensional (3D) nanostructures composed of hierarchically assembled subunits have demonstrated outstanding properties, compared with those of their bulk counterparts,[10] and studies on the shape-control synthesis of 3D iron oxide nanostructures are actively being pursued.[11−13] Of particular interest is the facile fabrication of hierarchical hollow structures assembled from low-dimensional subunits at the nanometer scale.[14−16]

Hematite (α-Fe_2O_3), an *n*-type semiconductor (E_g = 2.1 eV), is the most thermodynamically stable phase of iron oxide. α-Fe_2O_3 has been extensively used in catalysts, pigments, gas sensors, and energy storage.[17−20] Recently, many studies of α-Fe_2O_3 have been directed toward the fabrication of 3D-structured hollow α-Fe_2O_3 spheres as promising adsorbents for water treatment.[17,21−25] Although they have many advantageous properties, the majority of hollow α-Fe_2O_3 spheres have been prepared at elevated temperatures (higher than 180 °C) through hydro/solvothermal reactions over long periods of time. In addition, these synthesis methods typically involve the use of templates and toxic organic solvents, which result in high costs and hinder the practical application of the produced hollow α-Fe_2O_3 spheres in water treatment. Therefore, it is highly desirable to be able to fabricate α-Fe_2O_3 as hollow 3D nanostructures in a simple, eco-friendly, and cost-effective manner.

In this report, we describe a facile, green synthesis route for preparing hollow α-Fe_2O_3 nanostructures via a microwave-assisted, template-free, hydrothermal method. Compared with conventional synthetic methods using traditional heating at high temperature over many hours, the reaction is completed within 30 min using microwave heating at a relatively low temperature of 140 °C. This approach results in a synthesis route that is fast and energy-efficient. A possible mechanism for the formation of hollow structures is proposed based on a

Received: September 11, 2012
Accepted: November 6, 2012
Published: November 6, 2012

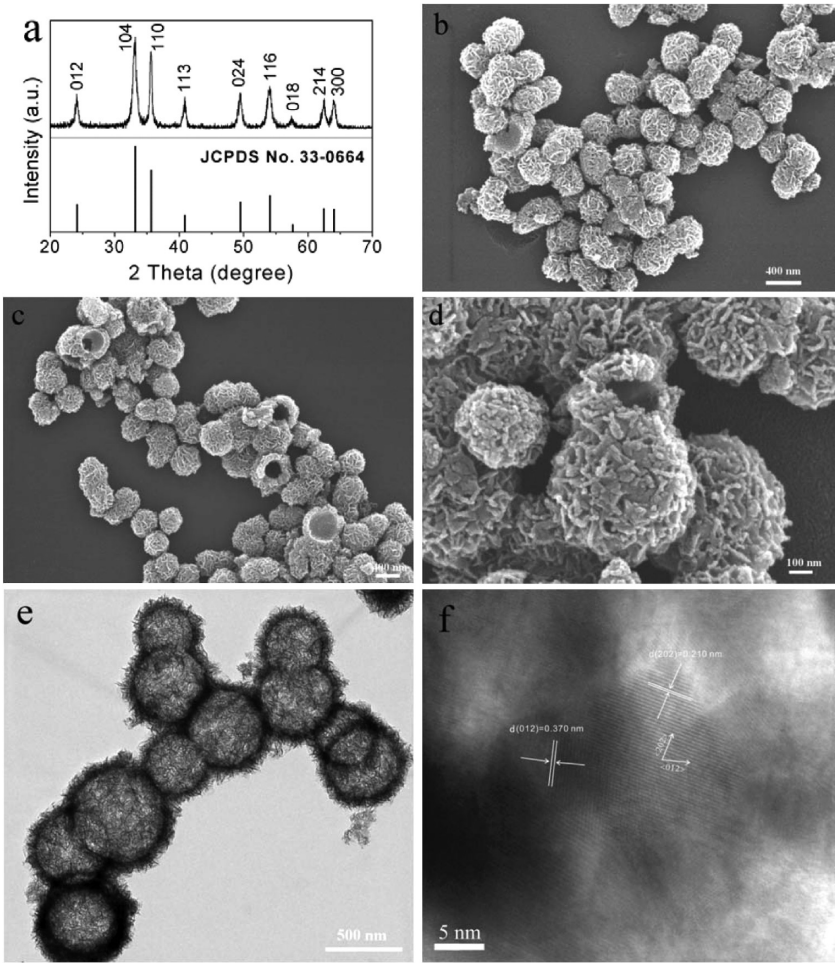

Figure 1. (a) XRD pattern, (b,c) low-magnification FESEM images, (d) high-magnification FESEM image, (e) TEM image, and (f) HRTEM image of the as-prepared hollow nestlike α-Fe_2O_3 nanostructures.

systematic investigation of the morphology of products prepared with different amounts of glycerol in the solvent. The obtained hollow α-Fe_2O_3 nanostructures exhibit excellent performance, with respect to the removal of As(V), Cr(VI), and Congo red from water.

2. EXPERIMENTAL SECTION

2.1. Synthesis of Hollow α-Fe_2O_3 Nanostructures. All reagents used were of analytical grade and purchased from Aldrich, unless otherwise noted. Ultrapure water with a resistivity of 18.2 MΩ cm^{-1}, produced using a Milli-Q apparatus (Millipore), was used in all of the experiments. In a typical procedure, 6 mmol $FeCl_3 \cdot 6H_2O$ and 6 mmol urea were dissolved in 60 mL of a mixture containing 15 mL of glycerol and 45 mL of water. After stirring and sonicating for 5 min, a transparent solution was obtained and then transferred to a 100-mL Teflon-lined autoclave. The autoclave was sealed and placed in a microwave synthesis system (MDS-6, Sineo, Shanghai, China), which was programmed to heat to 140 °C with a 30 min hold at this temperature. After heating, the autoclave was cooled naturally to room temperature. The red precipitate was collected, washed with water and ethanol several times by centrifugation, and then dried at 80 °C for 4 h.

2.2. Characterization. X-ray diffraction (XRD) measurements of the as-prepared product were collected using a Bruker D8 Avance X-ray diffractometer with Cu Kα irradiation (λ = 1.5406 Å) at room temperature. The surface morphology and structure were examined with a Hitachi S-4800 field-emission scanning electron microscopy (FESEM) system, using an acceleration voltage of 15 kV. Transmission electron microscopy (TEM) experiments were performed using a JEOL JEM-2100 instrument with an accelerating voltage of 200 kV. The as-prepared α-Fe_2O_3 powder was dispersed in ethanol, and a drop of the homogeneous dispersion was then loaded onto a carbon-coated copper grid and allowed to dry prior to analysis. N_2 adsorption and desorption isotherms were obtained using a Quantachrome Autosorb-1C system after the samples had been degassed under a flow of N_2 at 150 °C for 8 h.

2.3. Removal of Heavy-Metal Ions. Solutions with different concentrations (10, 20, 50, 100, 200, and 500 mg L^{-1}) of As(V) and Cr(VI) were prepared using $Na_2HAsO_4 \cdot 7H_2O$ and $K_2Cr_2O_7$, respectively. To obtain the adsorption isotherms, 15 mg of the hollow α-Fe_2O_3 nanostructures was added to 30 mL of the above solutions. After stirring at room temperature for 10 h, the solid and liquid phases were immediately separated, and the As(V) or Cr(VI) concentration in the remaining solutions was determined by inductively coupled plasma−optical emission spectroscopy (ICP-OES, Thermo-Fisher). The solutions with an initial As(V) and Cr(VI) concentration of 40 mg L^{-1} were used to study the adsorption rate. All of the adsorption experiments in

this study were performed in triplicate, and the mean values were used. The relative deviations were in the range of ±5.0%.

2.4. Removal of Selected Organic Pollutants. Congo red ($C_{32}H_{22}N_6O_6S_2Na_2$), which is an azo dye commonly used in the textile industry, was selected as a model organic water pollutant. Various amounts of the hollow α-Fe_2O_3 spheres were mixed with 20 mL of 100 mg L^{-1} Congo red solutions. After stirring for 10 h, the spheres were separated, and the supernatant solutions were analyzed by UV−vis spectroscopy (Shimadzu, Model 2550). The residual concentration of Congo red was obtained by integrating the area of the absorbance bands in the wavelength range of 400−600 nm using a linear calibration curve over 5−80 mg L^{-1}. The same experiments were performed using regenerated hollow α-Fe_2O_3 spheres and a commercial α-Fe_2O_3 powder that was purchased from BASF Chemicals (Tianjin, China).

3. RESULTS AND DISCUSSION

The chemical composition of the as-prepared product was analyzed using power XRD measurements. As shown in Figure 1a, all of the identified peaks could be unambiguously assigned to the hexagonal structure of α-Fe_2O_3 with structural parameters of $a = b = 5.038$ Å, $c = 13.772$ Å, which are in good agreement with the recorded values of JCPDS File Card No. 33-0664. No peaks from impurities were detected by XRD. The pronounced peaks at (012), (104), and (110) suggest that the obtained α-Fe_2O_3 was well-crystallized. According to the full width at the half-maximum of the diffraction peak, the average crystallite size can be estimated to be 10.6 nm, using the Scherrer equation:

$$D_{hkl} = \frac{K\lambda}{\beta_{hkl} \cos \theta_{hkl}}$$

where D_{hkl} is the crystallite size perpendicular to the normal line of the (hkl) plane, K a constant (0.89), β_{hkl} the full width at half-maximum (fwhm) of the (hkl) diffraction peak, θ_{hkl} the Bragg angle of the (hkl) peak, and λ the X-ray wavelength.

FESEM and TEM were also used to investigate the morphology of the as-prepared α-Fe_2O_3. As shown in Figures 1b and 1c, the product was composed of nestlike particles with an average diameter of ∼400 nm. The high-magnification FESEM image (Figure 1d) also shows that the nestlike spheres were comprised of nanorods measuring ∼20 nm in diameter and 100 nm in length. Several broken nanostructures in Figure 1c clearly reveal the hollow nature of the as-prepared α-Fe_2O_3 spheres. The corresponding TEM image (Figure 1e) confirms the formation of hollow nanostructures with a shell thickness of ∼60 nm. A representative high-resolution transmission electron microscopy (HRTEM) image of the α-Fe_2O_3 nanostructures (Figure 1f) shows the lattice image obtained at the edge of a sphere. The typical lattice fringe spacings were 0.370 and 0.210 nm, corresponding to the (012) and (202) planes of the hexagonal α-Fe_2O_3, respectively, which further indicates that the nanostructure consisted of single-crystalline nanoscale building blocks.

It has been reported that α-Fe_2O_3 micro/nano architectures with a solid-core structure can be obtained by processing at a relatively low temperature (120−150 °C) for 30 min, using microwave-assisted hydrothermal[26] (deionized water as the solvent) and solvothermal[22] (anhydrous ethanol as the solvent) reactions, when Fe^{3+} is used as the iron source and urea is the OH^- inducing agent. Although both methods have reduced the preparation time and do not involve organic templates or directing agents for fabricating α-Fe_2O_3 micro/nano architectures, they cannot produce products with hierarchically nanostructured hollow spheres. To investigate the formation mechanism of the as-prepared hollow α-Fe_2O_3 spheres, we studied the effect of the relative amounts of glycerol and water in the mixed solvent (60 mL) on the composition and morphology of the product. A series of experiments were performed by varying the volume of glycerol from 0 to 30 mL in the reaction while maintaining all other conditions constant.

The XRD patterns of the products prepared with different amounts of glycerol in a 60-mL glycerol−water mixed solvent (Figure 2) indicate that the products were also composed of α-

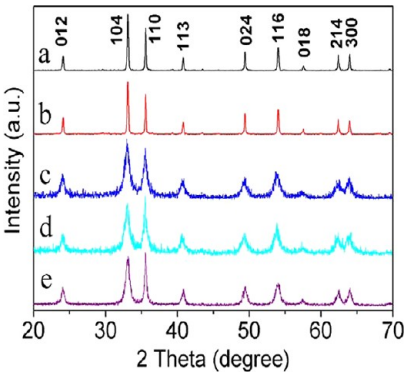

Figure 2. XRD patterns of the products obtained using different amounts of glycerol in the reaction system: (a) 0 mL, (b) 3 mL, (c) 6 mL, (d) 9 mL, and (e) 30 mL.

Fe_2O_3 (JCPDS File Card No. 33-0664), demonstrating that the relative amounts of glycerol and water in the mixed solvent did not affect the crystal form of the products. The narrow, sharp peaks in Figures 2a and 2b and the relatively broad and rough peaks in Figures 2c−e suggest that the α-Fe_2O_3 products prepared with an amount of glycerol no more than 3 mL in the mixed solvent were crystallized better than those prepared with a higher glycerol concentration. Calculated by the Scherrer equation, the average crystallite sizes of the α-Fe_2O_3 products represented by Figures 2a−e were 19.1, 18.4, 9.5, 9.8, and 11.2 nm, respectively. Furthermore, contrary to the data recorded in the standard card, the intensity of the (104) peak was slightly lower than that of the (110) peak in the products prepared with a mixed solvent containing 9 and 30 mL of glycerol, as shown in Figures 2d and 2e, respectively. This difference in the peaks was likely due to a trace amount of maghemite (γ-Fe_2O_3, JCPDS File Card No. 39-1346) existing in these two products. The (110) peak of α-Fe_2O_3 is at 35.61°, while the strongest (119) peak of maghemite is at 35.68°. The superposition of these two peaks resulted in an intensified peak at ∼35.65° that is stronger than the (104) peak. In fact, several peaks at 37.31°, 38.87°, and 50.08° are observable, although not distinct, in Figure 2d, which can be attributed to the (226), (209), and (2 1 12) peaks of the trace amount of maghemite. Interestingly, these phenomena were not observed when the volume of glycerol in the synthesis process was 15 mL, as shown in Figure 1a. This may be explained the fact that the product prepared under this condition had hollow cores, which render the subunits of the spheres more likely to fully contact the solvent during the thermal reaction, leading to the preferential formation of the more thermodynamically stable hematite.

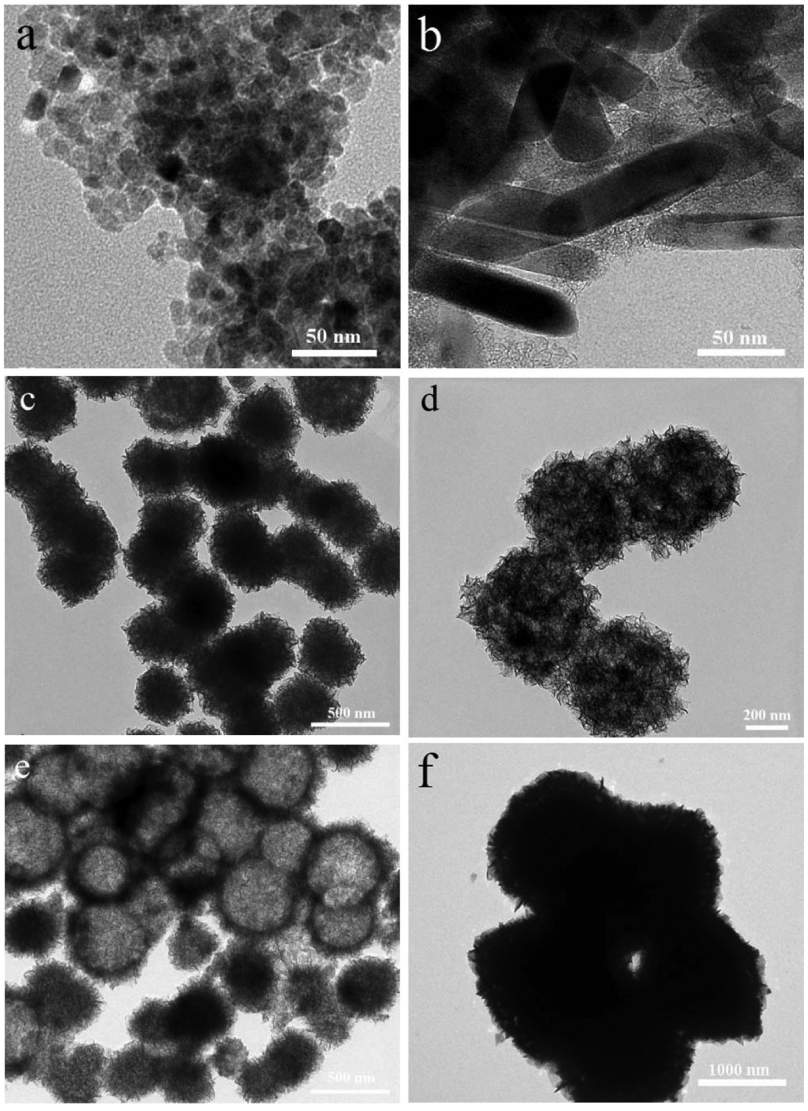

Figure 3. TEM images of the products obtained using different amounts of glycerol in the reaction system: (a) 0 mL, (b) 3 mL, (c) 6 mL, (d) 9 mL, (e) 15 mL, and (f) 30 mL.

Scheme 1. Schematic Illustration of the Formation Mechanism of a Hollow Nestlike α-Fe_2O_3 Nanostructure

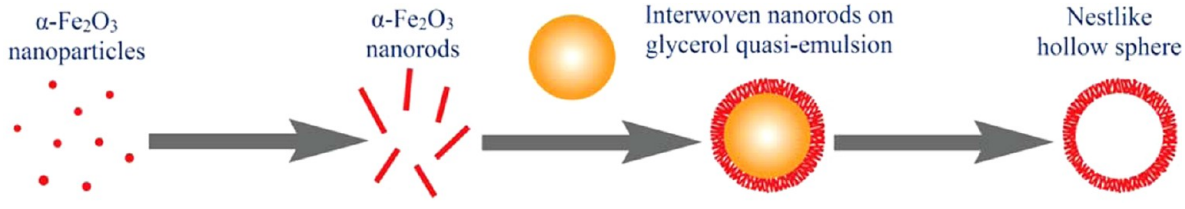

The TEM images shown in Figure 3 further illustrate the morphology of the products prepared with different amounts of glycerol. These data indicate that the effect of glycerol in the solvent on the morphology of α-Fe_2O_3 is highly dependent on the glycerol concentration. With pure water as the solvent, uniform granular crystals measuring ~10 nm in size were obtained (Figure 3a). When 3 mL of glycerol was added to the solvent, rodlike α-Fe_2O_3 structures with an average diameter of ~30 nm and a length of 50−100 nm were observed (Figure 3b). When the volume of glycerol was increased to 6 mL, agglomerations assembled from rodlike subunits were formed, as confirmed by the observation of solid irregular spheres with rough, "hairy" surfaces (Figure 3c). A further increase in the amount of glycerol to 9−15 mL led to the formation of relatively uniform spheres with partially hollow (Figures 3d and 3e) and completely hollow (Figure 1e) structures, which had an average diameter of ~400 nm. In particular, for a glycerol volume of 15 mL, the product contained hollow spheres with a more noticeable internal void space and more compactly assembled shells. When the volume of glycerol was further increased to 30 mL, large solid particles appeared, measuring 1500−2000 nm, which extensively agglomerated, as shown in Figure 3f.

dx.doi.org/10.1021/am301950k | ACS Appl. Mater. Interfaces 2013, 5, 598−604

The observations presented above indicate that the formation of hollow interiors in the as-prepared α-Fe_2O_3 hierarchical structures depends primarily on the volume ratio of glycerol and water in the reaction system. A possible formation mechanism is proposed in Scheme 1. We hypothesize that such a mechanism involves a quasi-microemulsion-assisted process similar to the formation of hollow α-FeOOH[27] and BiOBr[28] spheres. An appropriate amount of glycerol is mixed with water to form a uniform quasi-microemulsion, which is confirmed by the observed Tyndall effect of the mixed solvent (see Figure S1 in the Supporting Information). Although glycerol and water are miscible under thermodynamic equilibrium, it is reasonable to conceive that these polar solutes have a tendency to self-aggregate in aqueous media, thus forming microheterogeneities in the system.[29] These emulsified spheres serve as aggregation centers for the subsequent deposition of the shell structure. In one scenario, urea provides a steady but low supply of OH^- for Fe^{3+} to form $Fe(OH)_3$,[11] which immediately transforms to α-Fe_2O_3, because of rapid decomposition under microwave heating:

$$CO(NH_2)_2(s) + H_2O(l) \rightarrow 2NH_3(g) + CO_2(g) \quad (1)$$

$$NH_3(g) + H_2O(l) \rightarrow NH_4^+(aq) + OH^-(aq) \quad (2)$$

$$Fe^{3+}(aq) + 3OH^-(aq) \rightarrow Fe(OH)_3(s) \rightarrow \alpha\text{-}Fe_2O_3(s) \quad (3)$$

In another scenario, it is also possible for glycerol to be partially polymerized under hydrothermal conditions. In this case, the α-Fe_2O_3 nanoparticles would crystallize into rodlike nanostructures with the presence of glycerol in the solvent, where polymerized glycerol might serve as a directing agent, similar to the role played by poly(ethylene glycol) (PEG) described in previous reports.[30] Subsequently, these α-Fe_2O_3 nanorods would assemble on the surface of glycerol droplets to form compact shells. The outer α-Fe_2O_3 shells remain intact, whereas the inner glycerol droplets can be easily removed via solvent extraction during the rinsing and drying process, resulting in the formation of well-defined hollow spheres. Furthermore, a gradual release of micrometer/nanometer NH_3 and CO_2 bubbles due to the hydrolysis of urea and a gas–liquid equilibrium in the autoclave may also play an important role in the formation of the hollow spheres.[12,15]

The surface area and pore size distribution of the nestlike α-Fe_2O_3 nanostructures with completely hollow interiors were further determined by nitrogen adsorption–desorption measurements. Figure 4 shows a typical type IV isotherm with a hysteresis loop in the relative pressure range of 0.4–0.95, which suggests that the as-obtained nestlike α-Fe_2O_3 spheres are mesoporous materials. The Brunauer–Emmett–Teller (BET) surface area and the total pore volume of the nanostructures were calculated to be 152.42 $m^2\ g^{-1}$ and 0.42 $cm^3\ g^{-1}$, respectively, which are notably high values for iron oxide hierarchical nanostructures. Moreover, a sharp pore distribution with an average diameter of 3.8 nm was estimated by the Barrett–Joyner–Halenda (BJH) method. These pores likely resulted from the void space between the interwoven nanorods that constitute the hollow spheres.

It has been shown that hollow micro/nanostructured materials with high specific surface areas and ideal pore size distributions usually possess desirable adsorption properties for the removal of pollutants from water.[15,31,32] Here, we have evaluated the application of the as-prepared hollow nestlike α-Fe_2O_3 spheres to water treatment. Arsenic and chromium are typically considered highly toxic pollutants in water resources, and the efficient removal of these detrimental heavy-metal ions from water is of great importance. Figure 5a shows the

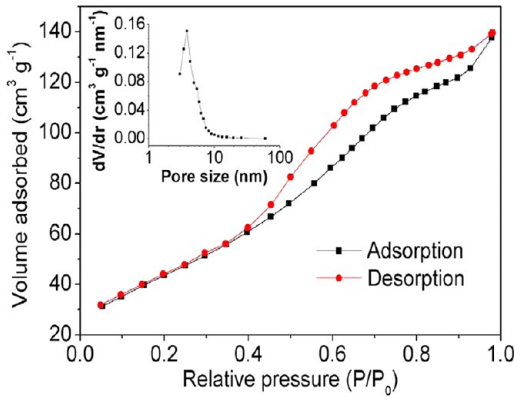

Figure 4. N_2 adsorption–desorption isotherm (inset: pore size distribution) of the hollow nestlike α-Fe_2O_3 nanostructures.

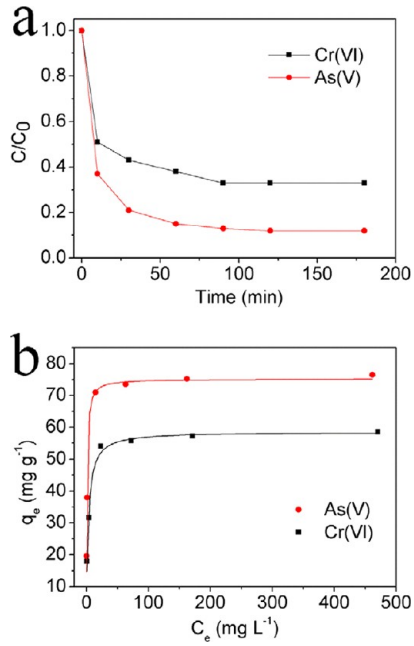

Figure 5. (a) Adsorption rate curves and (b) adsorption isotherms of As(V) and Cr(VI) using the hollow nestlike α-Fe_2O_3 nanostructures.

adsorption rates of As(V) and Cr(VI) ions with an initial concentration of 40 mg L^{-1} on the hollow nestlike α-Fe_2O_3 spheres. The adsorption processes were rapid during the initial 60 min, and the residual ratios of heavy-metal ions decreased very slowly thereafter with increasing time. The hollow spheres exhibited a superior capability for As(V) and Cr(VI) removal because equilibrium was established at high removal ratios (88% for As(V) and 67% for Cr(VI)) within 120 min. The Langmuir adsorption equation was selected to model the adsorption data over the concentration range of 0 to 500 mg L^{-1}:

$$q_e = \frac{q_m b C_e}{1 + b C_e}$$

dx.doi.org/10.1021/am301950k | ACS Appl. Mater. Interfaces 2013, 5, 598–604

where C_e (mg L^{-1}) is the equilibrium concentration of heavy-metal ions, q_e (mg g^{-1}) the amount of heavy-metal ions adsorbed per unit weight of the adsorbent at equilibrium, q_m (mg g^{-1}) the maximum adsorption capacity, and b the equilibrium constant related to the energy. Figure 5b shows that the experimental data fit well with the Langmuir adsorption model isotherms. Based on this isotherm, we calculated a maximum adsorption capacities of ~75.3 mg g^{-1} for As(V) and ~58.6 mg g^{-1} for Cr(VI) for the hollow nestlike α-Fe_2O_3 nanostructures. These values are much higher than those of previously reported nanomaterials, such as flower-like α-Fe_2O_3,[11,22] flower-like CeO_2,[33] hollow CeO_2 nanospheres,[34] chrysanthemum-like α-FeOOH microspheres,[7] and hollow urchin-like α-FeOOH spheres,[27] as listed in Table 1. These

Table 1. BET Surface Area and the Maximum As(V) and Cr(VI) Removal Capacities of Various Adsorbents

adsorbent sample	BET surface area (m^2 g^{-1})	maximum As(V) removal capacity (mg g^{-1})	maximum Cr(VI) removal capacity (mg g^{-1})	reference
hollow nestlike α-Fe_2O_3 spheres	152.42	75.3	58.6	this study
chrysanthemum-like α-FeOOH microspheres	120.8	66.2		7
flower-like α-Fe_2O_3	40	7.6	5.4	11
flower-like α-Fe_2O_3	130	51	30	22
hollow urchin-like α-FeOOH spheres	96.9	58		27
flower-like CeO_2	34	14.4	5.9	33
hollow CeO_2 nanospheres	72	22.4	15.4	34

results indicate that the as-obtained hollow nestlike α-Fe_2O_3 nanostructures have large adsorption capacities for As(V) and Cr(VI) and can be potentially used as an excellent adsorbent for As(V) and Cr(VI) in water treatment.

To further investigate the advantage of the hollow α-Fe_2O_3 nanostructures in water treatment, we studied the adsorption capabilities for Congo red (structure as shown in Figure S2 in the Supporting Information), a representative organic water pollutant. Congo red is typically absorbed onto the surface of metal oxides by coordination effect between metal ions and the amine groups at the ends of Congo red molecules. Figure 6a shows the adsorption spectra of the Congo red solutions (with an initial concentration of 100 mg L^{-1}) after treatment with different dosages of hollow α-Fe_2O_3 spheres for 10 h. The Congo red was almost completely removed from the water at an α-Fe_2O_3 dosage of 0.6 g L^{-1} (Figure 6a). Thus, a series of experiments were conducted using this dosage to determine the adsorption rate of Congo red on the hollow α-Fe_2O_3 spheres. As shown in Figures 6b and 6c, the as-prepared α-Fe_2O_3 was capable of removing ~90% of the Congo red within 50 min; with increasing time, the final efficiency of Congo red removal was up to 96% within 300 min without any additives at room temperature. The maximum adsorption capacity of the hollow nestlike α-Fe_2O_3 spheres for Congo red was calculated to be 160 mg g^{-1}. This ultrahigh removal efficiency could be largely attributed to the highly porous structure and large surface area of the spheres, as well as the electrostatic attraction between the

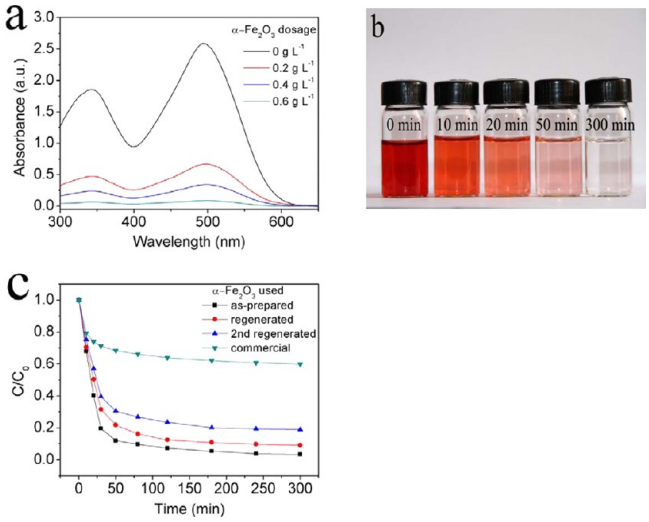

Figure 6. (a) UV–vis absorption spectra of Congo red solutions treated by different dosages of the as-prepared hollow α-Fe_2O_3 nanostructures, the initial concentration of Congo red is 100 mg L^{-1}; (b) picture of absorption of Congo red after different periods of time; and (c) adsorption rate of Congo red on the as-prepared and regenerated hollow α-Fe_2O_3 nanostructures and commercial α-Fe_2O_3.

α-Fe_2O_3 surfaces and Congo red. Table 2 shows the adsorption capacities of the hollow nestlike α-Fe_2O_3 spheres and those of

Table 2. BET Surface Area and the Maximum Congo Red Removal Capacity of Various Adsorbents

adsorbent sample	BET surface area (m^2 g^{-1})	maximum adsorption capacity for Congo red (mg g^{-1})	reference
hollow nestlike α-Fe_2O_3 spheres	152.42	160	this study
hollow boehmite microspheres	269	111.3	15
mesoporous α-Fe_2O_3	111	53	23
hierarchical hollow MnO_2 nanostructures		80	32
hollow urchin-like α-FeOOH nanostructures	239	239	35
hierarchical urchin-like α-Fe_2O_3 nanostructures	69	66	35
hierarchical spindle-like γ-Al_2O_3	149	90	36

certain previously reported materials. It appears that the adsorption capacity of the as-prepared α-Fe_2O_3 for Congo red is much higher than that the majority of similar materials.[15,23,27,32,35,36] Furthermore, the Congo red-adsorbed α-Fe_2O_3 particles can be renewed via catalytic combustion at 280 °C in air for 4 h,[32] and the renewed α-Fe_2O_3 particles exhibit a gradually decreasing Congo red removal efficiency with increasing regeneration time. However, even after being regenerated twice, the adsorption performance of the hollow α-Fe_2O_3 spheres toward Congo red is still much better than that of commercial α-Fe_2O_3, as shown in Figure 6c. It is worth noting that typical adsorption results reported in the literature are obtained under optimized conditions, including optimum pH, temperature, and adsorption time. Thus, it is conceivable that those reported high removal capacities and efficiencies

dx.doi.org/10.1021/am301950k | ACS Appl. Mater. Interfaces 2013, 5, 598–604

most likely cannot be achieved under practical conditions. Thus, because of the superior adsorption performance achieved without adjusting the process conditions, and the facile method of regeneration, the as-prepared hollow α-Fe_2O_3 spheres are a highly promising material that can be applied in water treatment systems for environmental protection.

CONCLUSIONS

In summary, hollow nestlike α-Fe_2O_3 nanostructures were successfully synthesized under microwave heating via a novel glycerol-assisted, template-free method. The relative amount of glycerol in the reaction system has a significant influence on the formation of hollow interiors in the products. The glycerol quasi-emulsion used in this study offers a "template" for the creation of interweaving α-Fe_2O_3 nanorods on the surfaces of the hollow nanostructures. It is likely that this process can be extended to the synthesis of other metal oxides with mesoporous hollow structures, and further studies are underway to broaden the applicability of this method. In water, the as-prepared hollow nestlike α-Fe_2O_3 spheres with mesoporous structures exhibit excellent adsorption capacities toward As(V) and Cr(VI) ions and Congo red that are much higher than those of most reported nanomaterials. We believe that these novel α-Fe_2O_3 hollow nanostructures may be applied as a promising adsorbent in water treatment.

ASSOCIATED CONTENT

Supporting Information

The observed Tyndall effect for the glycerol–water mixed solvent (Figure S1), and the molecular structure of Congo red (Figure S2). This information is available free of charge via the Internet at http://pubs.acs.org/.

AUTHOR INFORMATION

Corresponding Author

*Tel.: +86 532 82898707. Fax: +86 532 82968951. E-mail addresses: pcli@qdio.ac.cn (P.L.), xingronge@qdio.ac.cn (R.X.).

Notes

The authors declare no competing financial interest.

ACKNOWLEDGMENTS

This study was supported by the Science and Technology Development Program of Shandong Province (No. 2010GHY10514) and the National High Technology Research and Development Program ("863" Program) of China (No. 2011AA09070405).

REFERENCES

(1) Schwarzenbach, R. P.; Escher, B. I.; Fenner, K.; Hofstetter, T. B.; Johnson, C. A.; Gunten, U.; Wehrli, B. *Science* **2006**, *313*, 1702–1707.
(2) Hristovski, K. D.; Westerhoff, P. K.; Crittenden, J. C.; Olson, L. W. *Environ. Sci. Technol.* **2008**, *42*, 3786–3790.
(3) Cao, A.; Monnell, J. D.; Matranga, C.; wu, J.; Cao, L.; Gao, D. *J. Phys. Chem. C* **2007**, *111*, 18624–18628.
(4) Long, R. Q.; Yang, R. T. *J. Am. Chem. Soc.* **2001**, *123*, 2058–2059.
(5) Mishra, A. K.; Ramaprabhu, S. *J. Phys. Chem. C* **2010**, *114*, 2583–2590.
(6) Mou, F.; Guan, J.; Xiao, Z.; Sun, Z.; Shi, W.; Fan, X.-a. *J. Mater. Chem.* **2011**, *21*, 5414–5421.
(7) Li, H.; Li, W.; Zhang, Y.; Wang, T.; Wang, B.; Xu, W.; Jiang, L.; Song, W.; Shu, C.; Wang, C. *J. Mater. Chem.* **2011**, *21*, 7878–7881.
(8) Hu, J.-S.; Zhong, L.-S.; Song, W.-G.; Wan, L.-J. *Adv. Mater.* **2008**, *20*, 2977–2982.
(9) Deng, Y.; Qi, D.; Deng, C.; Zhang, X.; Zhao, D. *J. Am. Chem. Soc.* **2008**, *130*, 28–29.
(10) Hu, J.; Chen, M.; Fang, X.; Wu, L. *Chem. Soc. Rev.* **2011**, *40*, 5472–5491.
(11) Zhong, L. S.; Hu, J. S.; Liang, H. P.; Cao, A. M.; Song, W. G.; Wan, L. J. *Adv. Mater.* **2006**, *18*, 2426–2431.
(12) Lou, X. W.; Archer, L. A.; Yang, Z. *Adv. Mater.* **2008**, *20*, 3987–4019.
(13) Yu, J. G.; Guo, H.; Davis, S. A.; Mann, S. *Adv. Funct. Mater.* **2006**, *16*, 2035–2041.
(14) Yu, X.-Y.; Luo, T.; Jia, Y.; Zhang, Y.-X.; Liu, J.-H.; Huang, X.-J. *J. Phys. Chem. C* **2011**, *115*, 22242–22250.
(15) Cai, W.; Yu, J.; Cheng, B.; Su, B.-L.; Jaroniec, M. *J. Phys. Chem. C* **2009**, *113*, 14739–14746.
(16) Fan, H. J.; Gösele, U.; Zacharias, M. *Small* **2007**, *3*, 1660–1671.
(17) Lian, J.; Duan, X.; Ma, J.; Peng, P.; Kim, T.; Zheng, W. *ACS Nano* **2009**, *3*, 3749–3761.
(18) Fan, H. M.; You, G. J.; Li, Y.; Zheng, Z.; Tan, H. R.; Shen, Z. X.; Tang, S. H.; Feng, Y. P. *J. Phys. Chem. C* **2009**, *113*, 9928–9935.
(19) Du, D.; Cao, M. *J. Phys. Chem. C* **2008**, *112*, 10754–10758.
(20) Li, L.; Chu, Y.; Liu, Y.; Dong, L. *J. Phys. Chem. C* **2007**, *111*, 2123–2127.
(21) Cao, S.-W.; Zhu, Y.-J. *J. Phys. Chem. C* **2008**, *112*, 6253–6257.
(22) Cao, C. Y.; Qu, J.; Yan, W. S.; Zhu, J. F.; Wu, Z. Y.; Song, W. G. *Langmuir* **2012**, *28*, 4573–4579.
(23) Yu, C.; Dong, X.; Guo, L.; Li, J.; Qin, F.; Zhang, L.; Shi, J.; Yan, D. *J. Phys. Chem. C* **2008**, *112*, 13378–13382.
(24) Yu, J.; Yu, X.; Huang, B.; Zhang, X.; Dai, Y. *Cryst. Growth Des.* **2009**, *9*, 1474–1480.
(25) Xu, B.; Huang, B.; Cheng, H.; Wang, Z.; Qin, X.; Zhang, X.; Dai, Y. *Chem. Commun.* **2012**, *48*, 6529–6531.
(26) Qiu, G.; Huang, H.; Genuino, H.; Opembe, N.; Stafford, L.; Dharmarathna, S.; Suib, S. L. *J. Phys. Chem. C* **2011**, *115*, 19626–19631.
(27) Wang, B.; Wu, H.; Yu, L.; Xu, R.; Lim, T. T.; Lou, X. W. *Adv. Mater.* **2012**, *24*, 1111–1116.
(28) Cheng, H.; Huang, B.; Wang, Z.; Qin, X.; Zhang, X.; Dai, Y. *Chem.—Eur. J.* **2011**, *17*, 8039–8043.
(29) Wang, B.; Chen, J. S.; Wu, H. B.; Wang, Z.; Lou, X. W. *J. Am. Chem. Soc.* **2011**, *133*, 17146–17148.
(30) Zeng, Y.; Zhang, T.; Wang, L.; Wang, R. *J. Phys. Chem. C* **2009**, *113*, 3442–3448.
(31) Jiang, S.-D.; Yao, Q.-Z.; Zhou, G.-T.; Fu, S.-Q. *J. Phys. Chem. C* **2012**, *116*, 4484–4492.
(32) Fei, J. B.; Cui, Y.; Yan, X. H.; Qi, W.; Yang, Y.; Wang, K. W.; He, Q.; Li, J. B. *Adv. Mater.* **2008**, *20*, 452–456.
(33) Zhong, L.-S.; Hu, J.-S.; Cao, A.-M.; Liu, Q.; Song, W.-G.; Wan, L.-J. *Chem. Mater.* **2007**, *19*, 1648–1655.
(34) Cao, C.-Y.; Cui, Z.-M.; Chen, C.-Q.; Song, W.-G.; Cai, W. *J. Phys. Chem. C* **2010**, *114*, 9865–9870.
(35) Fei, J.; Cui, Y.; Zhao, J.; Gao, L.; Yang, Y.; Li, J. *J. Mater. Chem.* **2011**, *21*, 11742–11746.
(36) Cai, W.; Yu, J.; Jaroniec, M. *J. Mater. Chem.* **2010**, *20*, 4587–4594.